Research Square

Preprints are preliminary reports that have not undergone peer review.
They should not be considered conclusive, used to inform clinical practice,
or referenced by the media as validated information.

Positioning-Oriented Calibration of Near-Field Antenna Arrays

Sajad Daei

sajado@kth.se

KTH Royal Institute of Technology

Gabor Fodor

KTH Royal Institute of Technology

Mikael Skoglund

KTH Royal Institute of Technology

Article

Keywords:

Posted Date: November 16th, 2026

DOI: https://doi.org/10.21203/rs.3.rs-11526566/v1

License: This work is licensed under a Creative Commons Attribution 4.0 International License.
Read Full License

Additional Declarations: No competing interests reported.

Positioning-Oriented Calibration of Near-Field Antenna Arrays

Sajad Daei[1,*], Gábor Fodor[1,2], and Mikael Skoglund[1]

[1]Division of Information Science and Engineering, KTH Royal Institute of Technology, Stockholm, Sweden
[2]Ericsson Research, Stockholm, Sweden
[*]Correspondence: sajado@kth.se

Abstract. Near-field arrays estimate position from wavefront curvature and relative received amplitudes. Unknown receiver phases and delays can obscure the phase information, making calibration a positioning design problem. We study which noisy calibration measurements are most useful when sensing and calibration share a finite received signal-to-noise ratio budget. Under a spherical-wave model with known relative receiver gains and known reference-path responses, we separate position information into amplitude and calibrated phase contributions. This yields a geometry condition for nonsingular local information and shows how reference frequencies constrain receiver phase at the sensing carrier. We then allocate resources between sensing and selected sensor pairs by convex optimization. Comparisons with uniform calibration designs and simulations of complex observations demonstrate the resulting accuracy gains. The framework distinguishes calibration needed for local identifiability from calibration needed for useful positioning accuracy.

Keywords: array calibration; calibration graphs; experimental design; Fisher information; near-field positioning; sensor delays.

1 Introduction

Wireless networks are evolving beyond their traditional role of providing connectivity towards supporting spatially aware services, including positioning and integrated sensing and communication [1]. This evolution is reflected in the IMT-2030 framework, which recognizes sensing-related capabilities as an important dimension of future wireless systems. As wireless infrastructure is increasingly expected to infer the locations of devices and objects, the design of its underlying signal processing and hardware-support functions must also account for the requirements of these emerging services [2, 3].

Array calibration is a key hardware-support function that is typically designed to characterize and compensate hardware-induced gain, phase and timing uncertainties to support coherent reception, beamforming and reliable communication [4]. These objectives remain essential, but positioning introduces an additional consideration: calibration quality should also be evaluated in terms of its contribution to spatial estimation accuracy. In particular, calibration measurements that are effective for estimating receiver hardware parameters are not necessarily equally valuable for positioning. The reason is that positioning accuracy depends not only on the uncertainty of the hardware parameters, but also on how source motion changes the received signals across the array. Consequently, the value of a calibration measurement depends on the propagation geometry and the positioning task.

This distinction becomes particularly relevant in near-field positioning and sensing [5, 6]. A receive array can estimate the direction of a nearby source from phase differences across its sensors. Wavefront curvature also makes these differences depend on range. The received amplitudes vary with the sensor - source distances and provide another source of position information. Receiver errors affect the two differently: unknown channel phases can hide the phase changes caused by source motion, but they leave amplitude ratios unchanged. With known relative receiver gains, amplitude ratios can provide nonsingular local position information even without phase calibration. However, this information may be too weak for useful accuracy. These observations motivate a positioning-oriented calibration approach in which the selection and quality of calibration measurements are determined by their contribution to position accuracy, rather than by hardware-parameter estimation accuracy alone. We therefore ask how much phase calibration improves position accuracy, which reference frequencies and sensor pairs should be measured, and how a finite budget should be divided between calibration and sensing.

Curvature-based ranging and amplitude-based localization are established ideas. Zhang et al. relate spherical-wave positioning to curvature of arrival [7]. Begriche et al. derive exact near-field bounds with both equal and distance-dependent sensor amplitudes [8]. He et al. recover bearing and range from exact spatial amplitude and phase responses; their magnitude-based estimator assumes magnitude-calibrated sensors [9]. Gazzah and Delmas study array geometry design [10], and Wymeersch analyses joint localization and synchronization [11]. These studies explain how spatial amplitude and phase variations carry position information. They provide the foundation for assessing how hardware calibration affects the position information available from near-field observations.

Calibration and localization have also been studied jointly. He et al. estimate mixed near- and far-field sources using three fully calibrated sensors and subsequently calibrate the remaining gain and phase responses [12]. Ramamohan et al. develop joint gain, phase and direction-of-arrival estimation methods and identifiability conditions for acoustic arrays [13]. Yang et al. study sensor-phase self-calibration [14]. These studies show how hardware assumptions affect localization, including cases in which only part of the array is calibrated

beforehand.

Other studies examine what calibration measurements themselves can provide. Larsson relates pairwise reciprocity-calibration accuracy to a graph and analyses its consequences for coherent beamforming and scalability [15]. Wu et al. estimate phase and time offsets from wideband inter-antenna observations, including line-of-sight and reflected paths under different location and map assumptions [16]. Qing Zhang et al. analyze orthogonal frequency-division multiplexing (OFDM) localization bounds and spatial ambiguities under phase offsets, and validate channel state information (CSI) calibration experimentally [17]. These complementary research directions establish the importance of near-field propagation, hardware uncertainty and calibration measurements. They also motivate a further design question: rather than evaluating calibration solely through the accuracy of recovered hardware parameters, how should calibration measurements be selected and weighted to improve positioning accuracy under a limited measurement budget? In particular, a calibration link that strongly constrains receiver phase differences need not provide the greatest improvement in positioning, because its value also depends on the sensitivity of those phase differences to source displacement.

To address this question, we develop a positioning-oriented calibration framework that treats noisy hardware-reference measurements as part of the observation model and the measurement budget. Our reference measures hardware phase differences between selected receiver pairs at chosen frequencies. Its path phase and observation amplitude are known. Each receiver has an unknown phase offset and delay, with a known relative magnitude response. The source is observed at one carrier frequency using a spherical-wave model with inverse-distance amplitudes. We measure resources by received signal-to-noise ratio (SNR): the budget is the sum of the sensing and reference SNRs. We assess local accuracy through the Fisher information matrix (FIM), which describes the sensitivity of the observations to small parameter changes.

Our analysis establishes three main results. First, we characterize how receiver calibration contributes to near-field positioning information. Theorem 1 gives an exact position FIM after eliminating the unknown common gain, receiver phases and delay slopes. It separates the information in relative amplitudes from the information in phase differences supported by calibration. The expression shows how reference frequencies and pair weights affect position accuracy, including for disconnected graphs and unequal received sensor powers.

Second, we establish when the available amplitude and calibrated phase information is sufficient for local positioning, showing that complete calibration-graph connectivity is not always necessary. Proposition 1 gives the condition under which amplitude changes and calibrated phase differences jointly constrain every position coordinate. It explains why a disconnected calibration graph can suffice and why amplitude information remains when a single off-carrier reference supplies no carrier-phase information. For a line array with at least three distinct sensor positions and a source off the sensor line, Proposition 2 shows that the amplitude term alone has full local rank under the stated magnitude-calibration assumption. Importantly, local identifiability does not by itself guarantee useful positioning accuracy, which motivates the design of calibration measurements according to their quantitative contribution to the position-error bound.

Third, we develop an information-aware allocation of calibration resources that directly targets positioning accuracy. Proposition 4 uses this FIM to allocate received SNR between sensing and individual reference pairs. The allocation minimizes average position variance over a set of anticipated source locations. The problem is convex, and a Frank-Wolfe gap bounds how far a computed design is from the optimum. In the numerical comparison, each uniform baseline has its own optimized sensing share. The reported improvements therefore include the benefit of choosing the pair weights after optimizing the sensing/calibration split.

The frequency rule follows classical intercept estimation [18], and the allocation uses established convex design and Frank-Wolfe methods [19, 20]. We check the information formula against an independently assembled observation Jacobian and assess the designs with a standard joint likelihood fit. The estimator serves to test the design predictions. The numerical results demonstrate that allocating calibration resources according to their positioning value can improve accuracy compared with uniform calibration graphs under the same received-SNR budget.

Our earlier *When Near Becomes Far* paper chooses propagation-model boundaries from mismatch tolerances [21]. Our continuous range-angle recovery work studies reconstruction from structured or compressed measurements [22–25]. Here we choose noisy hardware-reference measurements to improve position accuracy. The results concern local accuracy; reflection and phase-wrapping ambiguities require separate analysis [26]. Table 1 compares the observation assumptions and results with the closest prior work.

2 Results

Vectors and matrices are bold; $\mathbb{R}$ and $\mathbb{C}$ denote the real and complex numbers. The symbol $\mathbb{E}$ denotes expectation. Superscripts T and H denote transpose and conjugate transpose. The norm $\|\cdot\|$ is Euclidean, $j^2 = -1$, $\mathbf{I}_n$ is the n-dimensional identity matrix, and $\mathbf{1}$ is an all-ones vector of the required size. For a vector, diag forms a diagonal matrix; tr sums the diagonal entries of a matrix; and rank counts its independent columns.

2.1 Spherical-wave sensing and coherent calibration

Consider N sensors at known positions $\mathbf{p}_m \in \mathbb{R}^2$, $m = 1, \ldots, N$, and a source at $\mathbf{x} \in \mathbb{R}^2$. We use $d = 2$ spatial coordinates throughout. The source lies in a specified half-plane, which is the upper half-plane in the line-array examples. It does not coincide with a sensor or the coordinate origin. The sensor distances and their

Table 1: Relation to prior work. Relative receiver magnitudes and reference-path phases are known in the present model.

Prior study	Established problem and output	Specific result in this paper
Begriche et al. [8]; He et al. [9]	Exact spherical-wave bounds and position recovery using spatial amplitude and phase variation.	Add a separate noisy reference likelihood, eliminate receiver phase and delay uncertainty, and express its contribution to position information.
He et al. [12]; Ramamohan et al. [13]	Localization with partly calibrated arrays; joint hardware/source estimation and self-calibration conditions.	Test local position rank using both amplitude geometry and phase differences supplied by selected noisy reference pairs.
Larsson [15]	Graph-based reciprocity-calibration accuracy and its effect on coherent beamforming and network scalability.	Map receive-phase reference information through source-position sensitivities, including the amplitude contribution and unknown delay slopes.
Wu et al. [16]	Wideband phase/time calibration with direct and reflected paths, location/map assumptions, estimators and bounds.	Under controlled known reference paths, reduce frequency placement to carrier-phase information and allocate received SNR over pairs and sensing.
Qing Zhang et al. [17]	OFDM localization bounds, spatial ambiguity analysis and experimentally validated CSI phase calibration.	Design reference frequencies, pair weights and the sensing/reference SNR split for an average local position bound; validation here is simulated.
Our propagation and recovery work [21–25]	Mismatch-tolerance boundaries and continuous source recovery for specified propagation/measurement models.	Choose noisy calibration measurements under an explicit hardware model and a shared received-SNR budget.

differences from the distance to the origin are

$$\begin{aligned} r_m &= \|\mathbf{x}-\mathbf{p}_m\|, \quad r = \|\mathbf{x}\|, \\ \delta_m &= r_m - r, \qquad k_0 = 2\pi f_0/c, \\ \mathbf{G}_{m,:} &= \frac{(\mathbf{x}-\mathbf{p}_m)^T}{r_m} - \frac{\mathbf{x}^T}{r}. \end{aligned} \tag{1}$$

Here f_0 is the sensing carrier and c is the propagation speed. The quantity k_0 is the carrier wavenumber. For the line-array examples, we write $\mathbf{x} = r[\cos\theta, \sin\theta]^T$, where θ is measured counterclockwise from the positive array axis. The coordinate origin is only a phase reference; no sensor is required there. Define $\boldsymbol{\delta} = [\delta_1, \ldots, \delta_N]^T$. Row m of the Jacobian $\mathbf{G} \in \mathbb{R}^{N\times d}$ is the position gradient of δ_m, so $\mathbf{G}\mathbf{v}$ is the first-order change in these path differences caused by a small source displacement $\mathbf{v}$.

For identical isotropic receive responses, a scalar free-space field has amplitude proportional to $1/r_m$. Define normalized amplitudes and the steering vector by

$$\omega_m(\mathbf{x}) = \frac{r_m^{-2}}{\sum_{n=1}^{N} r_n^{-2}}, \qquad m = 1, \ldots, N,$$

$$A_m(\mathbf{x}) = \sqrt{N\omega_m(\mathbf{x})}, \tag{2}$$

$$[\mathbf{a}_{\mathrm{NF}}(\mathbf{x})]_m = A_m e^{-jk_0\delta_m}. \tag{3}$$

The dimensionless weight $\omega_m(\mathbf{x})$ is sensor m's fraction of the total received sensing SNR, with $\sum_m \omega_m(\mathbf{x}) = 1$. We suppress the position dependence of r_m, A_m and ω_m below. This normalization gives $\|\mathbf{a}_{\mathrm{NF}}\|^2 = N$ and preserves all amplitude ratios, since $A_m/A_j = r_j/r_m$. The common distance-dependent magnitude is absorbed into the unknown complex gain. To see the connection with the unnormalized field, let β be its common coefficient. Then $\beta r_m^{-1} e^{-jk_0 r_m} = \alpha A_m e^{-jk_0\delta_m}$ when

$$\alpha = \frac{\beta e^{-jk_0 r}}{\sqrt{N}} \sqrt{\sum_j r_j^{-2}}.$$

Thus the normalized and unnormalized fields describe the same sensor responses when their common gain is unknown.

Let ψ_m be receiver m's unknown hardware phase at the sensing carrier, and stack these phases as $\boldsymbol{\psi} = [\psi_1, \ldots, \psi_N]^T$. Define $\mathbf{D}(\boldsymbol{\psi}) = \mathrm{diag}(e^{j\psi_1}, \ldots, e^{j\psi_N})$. Each y_m is one complex baseband observation. With $\mathbf{y} = [y_1, \ldots, y_N]^T \in \mathbb{C}^N$, noise vector $\mathbf{n} \in \mathbb{C}^N$ and unknown common gain $\alpha \in \mathbb{C}$, the sensing model is

$$\mathbf{y} = \alpha\mathbf{D}(\boldsymbol{\psi})\mathbf{a}_{\mathrm{NF}}(\mathbf{x}) + \mathbf{n}, \quad \mathbf{n} \sim \mathcal{CN}(\mathbf{0}, \mathbf{I}_N), \tag{4}$$

The notation $\mathcal{CN}(\mathbf{0}, \mathbf{I}_N)$ denotes zero-mean proper complex Gaussian noise with covariance $\mathbf{I}_N$; each sensor noise has $\mathbb{E}|n_m|^2 = 1$. In scalar form, $y_m = \alpha A_m e^{-jk_0\delta_m + j\psi_m} + n_m$. The total received sensing SNR is $S = N|\alpha|^2$, and sensor m receives SNR $S\omega_m$. At each design point, S specifies the total SNR received by the array. Keeping S fixed across positions therefore compares received observation quality. The required transmit power may vary with position.

The displayed model assumes equal, known receiver magnitude gains. This assumption allows amplitude ratios to reflect differences in propagation distance. Unknown sensor gains could instead imitate the amplitude changes caused by source motion. The Discussion examines this case. The unit noise covariance assumes equal receiver noise variances. Unequal variances can be treated by whitening, provided the signal and calibration models are transformed consistently.

Each receiver has an unknown phase offset ϕ_m and a path-equivalent delay error ϵ_m, measured in metres; the corresponding delay is ϵ_m/c seconds. At frequency

f, and with positive frequency scale B_r in hertz, write

$$\phi_m - 2\pi f \epsilon_m / c = \psi_m + u\chi_m, \qquad (5)$$
$$u = (f - f_0)/B_r, \quad \chi_m = -2\pi B_r \epsilon_m / c,$$

so $\psi_m = \phi_m - k_0\epsilon_m$ is the hardware phase at the sensing carrier. The errors remain constant during sensing and calibration. The offset u is dimensionless, and χ_m is the phase slope with respect to u. Choosing B_r sets the units of this slope while leaving the physical frequency response unchanged. Write $\boldsymbol{\chi} = [\chi_1, \ldots, \chi_N]^T$.

Let $\mathcal{E}$ be the set of candidate sensor pairs. For $e = (i, j) \in \mathcal{E}$, set $\mathbf{b}_e = \mathbf{e}_i - \mathbf{e}_j$, where $\mathbf{e}_i$ is the ith standard basis vector in $\mathbb{R}^N$. The incidence matrix $\mathbf{B} \in \mathbb{R}^{|\mathcal{E}| \times N}$ stacks the rows $\mathbf{b}_e^T$.

Use reference frequencies f_ℓ, $\ell = 1, \ldots, L_f$, with normalized offsets $u_\ell = (f_\ell - f_0)/B_r$. Assign pair e received reference SNR $q_e \geq 0$, and split it over frequencies using fixed weights $w_\ell \geq 0$ with $\sum_\ell w_\ell = 1$. The same frequency weights apply to all pairs. Stack the pair budgets as $\mathbf{q} = (q_e)_{e \in \mathcal{E}}$. After removing the known reference-path response, the coherent reference observation is

$$z_{e\ell} = \sqrt{q_e w_\ell}\, e^{j\mathbf{b}_e^T(\boldsymbol{\psi} + u_\ell \boldsymbol{\chi})} + v_{e\ell}, \quad v_{e\ell} \sim \mathcal{CN}(0, 1). \quad (6)$$

The sample $z_{e\ell}$ measures pair e at tone ℓ, and $v_{e\ell}$ is its noise. All sensing and reference noises are independent. This model assumes known reference-path phases and observation amplitudes. If each link had an independent unknown path phase, the reference could no longer distinguish that phase from the receiver phase difference. Equation (6) assumes a direct noisy observation of a hardware phase difference. If this observation is formed from ratios or correlations of noisy receiver samples, its noise distribution and dependence must be established before applying the information formula. The active calibration graph has one node per sensor and an edge for every pair with $q_e > 0$. It is connected when a path of active edges joins every two sensors. Its weighted Laplacian is $\mathbf{L} = \mathbf{B}^T \operatorname{diag}(\mathbf{q})\mathbf{B}$. We compare allocations at fixed total received SNR

$$T = S + Q, \qquad Q = \sum_e q_e. \qquad (7)$$

The SNRs S, Q and T are in linear units; a total budget reported in decibels is $10 \log_{10} T$ dB. The budget counts received observation quality. It does not account for the transmit energy needed to overcome reference-path losses, or for acquisition time, transport and switching costs. These costs depend on how the reference is implemented.

2.2 Position information from amplitude and calibrated phase

We first describe how a small source displacement changes the received amplitudes. Let $\boldsymbol{\omega} = [\omega_1, \ldots, \omega_N]^T$ collect the sensor-power weights. The logarithmic amplitude derivatives and their information weights are

$$\mathbf{R}_{m,:} = \nabla_{\mathbf{x}}^T \log(r_m^{-1}) = -\frac{(\mathbf{x} - \mathbf{p}_m)^T}{r_m^2}, \qquad (8)$$

$$\mathbf{P}_\omega = \operatorname{diag}(\boldsymbol{\omega}) - \boldsymbol{\omega}\boldsymbol{\omega}^T, \qquad \mathbf{K} = 2S\mathbf{P}_\omega. \qquad (9)$$

Here ker denotes the nullspace and span$\{\mathbf{1}\}$ consists of constant vectors. Because all $\omega_m > 0$, $\ker \mathbf{P}_\omega = \operatorname{span}\{\mathbf{1}\}$. The ordinary centering matrix $\mathbf{C} = \mathbf{I} - \mathbf{1}\mathbf{1}^T/N$ subtracts the sensor average. We use it later to state a rank condition. The matrix $\mathbf{P}_\omega$ accounts for the unequal received sensor powers. Differentiating the normalized amplitude gives

$$\nabla_{\mathbf{x}}^T \log A_m = \mathbf{R}_{m,:} - \boldsymbol{\omega}^T \mathbf{R}. \qquad (10)$$

The reference must separate the hardware phase at the sensing carrier from the unknown delay slope. Let μ and ν be the first and second weighted moments of its normalized frequency offsets, and define

$$\mu = \sum_\ell w_\ell u_\ell, \quad \nu = \sum_\ell w_\ell u_\ell^2,$$
$$\gamma = \begin{cases} 1 - \mu^2/\nu, & \nu > 0, \\ 1, & \nu = 0, \end{cases} \qquad \boldsymbol{\Lambda} = 2\gamma\mathbf{L}. \qquad (11)$$

The factor $\gamma \in [0, 1]$ compares the carrier-phase information available when the delay slopes are unknown with that available from the same reference measurements and SNRs when the slopes are known. Thus $\gamma = 1$ means that the unknown slopes cause no information loss, while $\gamma = 0$ means that no carrier-phase information remains after accounting for them. The remaining hardware-phase FIM is $\boldsymbol{\Lambda} = 2\gamma\mathbf{L}$. Since $u = 0$ is the sensing carrier, ψ_m is the intercept of the receiver's affine phase response. The derivation is given in Section 4.1.1.

Uncertainty in the common gain and hardware parameters affects position accuracy. We treat them as nuisance parameters and write $\mathbf{J}_{\mathbf{x}}$ for the position FIM that remains after accounting for them. At a regular point with $\mathbf{J}_{\mathbf{x}} \succ 0$, its inverse is the Cramér-Rao covariance bound for locally unbiased position estimation. Define the position-error bound (PEB) as

$$\operatorname{PEB}(\mathbf{x}) = \sqrt{\operatorname{tr}(\mathbf{J}_{\mathbf{x}}^{-1})}. \qquad (12)$$

The PEB describes the local accuracy limit under this model; measured estimation errors are reported separately. We use $\succ 0$ for positive definiteness, $\succeq 0$ for positive semidefiniteness, and $\dagger$ for the Moore-Penrose pseudoinverse. For a symmetric matrix, this pseudoinverse inverts nonzero eigenvalues and leaves zero eigenvalues at zero.

A source displacement changes both amplitudes and phases. The references limit which phase changes the unknown receiver phases can absorb. The following result gives the position information that remains after accounting for the unknown parameters.

Theorem 1. *For $S > 0$, the equivalent position FIM for (4)-(6), with unknown common gain, receiver carrier phases and delay slopes, is*

$$\mathbf{J}_{\mathbf{x}} = \mathbf{J}_A + k_0^2 \mathbf{G}^T \mathbf{W} \mathbf{G}, \qquad (13)$$
$$\mathbf{J}_A = \mathbf{R}^T \mathbf{K} \mathbf{R},$$
$$\mathbf{W} = \mathbf{K} - \mathbf{K}(\mathbf{K} + \boldsymbol{\Lambda})^\dagger \mathbf{K}.$$

Both terms are positive semidefinite.

Here $\mathbf{J}_A$ is the information in relative received amplitudes. The phase term depends on the position sensitivity $\mathbf{G}$ and the matrix $\mathbf{W}$. The latter combines the sensing weights $\mathbf{K}$ with the reference information $\mathbf{\Lambda}$ to determine how much phase information remains after the unknown receiver phases are eliminated. Calibration therefore affects the phase contribution through $\mathbf{W}$.

Amplitude and phase perturbations contribute separately under the complex Gaussian noise model. Eliminating the unknown common gain removes the common amplitude and phase components, while the references constrain the remaining hardware phase differences. The full derivation is given in Section 4.1.1.

Equation (13) connects the measurement choices to position accuracy. The frequencies determine γ, while the measured pairs and their SNRs determine $\mathbf{L}$. Source and array geometry enter through $\mathbf{G}$ and $\mathbf{R}$, and the received sensor powers enter through $\mathbf{K}$. We can therefore compare reference designs using the position bound itself.

At fixed sensing SNR, stronger reference measurements increase the phase term. With no informative references, $\mathbf{\Lambda} = 0$ and $\mathbf{W} = 0$, so $\mathbf{J}_{\mathbf{x}} = \mathbf{J}_A$. As calibration constrains all relative phases with increasing precision, the information tends to $\mathbf{J}_A + k_0^2 \mathbf{G}^T \mathbf{K} \mathbf{G}$. The amplitude term depends on distance through $\mathbf{R}$; the phase term also carries the carrier-wavenumber factor k_0^2.

The phase-only formula follows by using an equal-amplitude model: set $A_m = 1$ for every position and discard the amplitude derivatives. This gives $\mathbf{J}_A = 0$ and $\mathbf{K} = (2S/N)\mathbf{C}$. Equal received powers at a single position do not justify discarding their derivatives, because a displacement can still change them. Under spherical spreading, $\mathbf{K}$ and $\mathbf{\Lambda}$ need not commute. They therefore cannot generally be treated through a common scalar eigenvalue rule.

2.3 Which calibration constraints are sufficient?

The information formula lets us ask whether any small source displacement remains unobserved. Such a displacement must preserve the amplitude ratios and the phase differences constrained by the references. Let $\mathcal{A} = \{e \in \mathcal{E} : q_e > 0\}$ be the active pairs and let $\mathbf{B}_{\mathcal{A}}$ contain their rows of $\mathbf{B}$. Using the centering matrix $\mathbf{C}$ defined above, these two requirements give the following condition.

Proposition 1. *For $S > 0$ and $\gamma > 0$,*

$$\mathbf{J}_{\mathbf{x}} \succ 0 \quad \Longleftrightarrow \quad \operatorname{rank} \begin{bmatrix} \mathbf{CR} \\ \mathbf{B}_{\mathcal{A}} \mathbf{G} \end{bmatrix} = d, \tag{14}$$

For $S > 0$, if $\gamma = 0$ or $q_e = 0$ for every candidate pair $e \in \mathcal{E}$, the condition is $\operatorname{rank}(\mathbf{CR}) = d$.

The proof in Section 4.1.2 identifies the source displacements that neither amplitude changes nor calibrated phase differences can distinguish.

A displacement is detectable if it changes either the relative amplitudes or a phase difference supported by calibration. This can happen even when some hardware phase differences are unobserved. A connected graph constrains every relative phase. If $\operatorname{rank}(\mathbf{CG}) = d$, these phase constraints alone provide nonsingular local position information. A disconnected graph can also suffice because amplitudes may constrain the remaining displacement directions, or all of them. The condition concerns small displacements around the true position; unique recovery over the full search region needs a separate analysis.

For a line array, the amplitude part alone can satisfy the rank condition. The next result identifies a simple geometry in which this happens.

Proposition 2. *For at least three sensors at distinct positions $(s_m, 0)$ and a source (x, y) with $y \neq 0$, the amplitude term $\mathbf{J}_A$ is positive definite when relative sensor magnitudes are known and $S > 0$.*

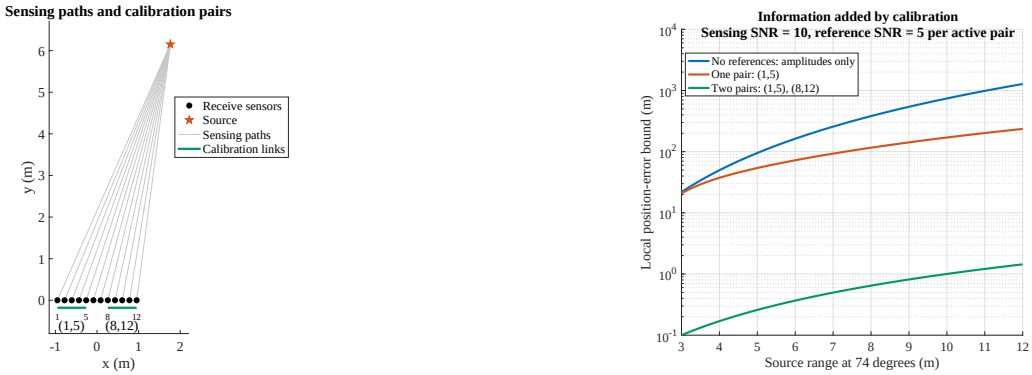
A short polynomial argument establishes this result; the proof is given in Section 4.1.3.

Full local rank can coexist with poor accuracy: the smallest eigenvalue of $\mathbf{J}_A$ may be very small at the available SNR. The mirror positions on opposite sides of the sensor line also have the same amplitudes. Magnitude-based near-field localization is established [9]. This result shows why the present model can retain local position information without phase calibration, while the numerical study below shows how weak that information can be. Figure 1 illustrates the distinction between local rank and positioning accuracy. Panel a shows two disconnected calibration pairs. Panel b shows that these references improve the position-error bound even though amplitude information already provides full local rank. Sensing SNR is fixed in this comparison; adding reference measurements increases the total received-SNR budget. For the line array used in the numerical study, calibration is therefore needed to improve accuracy, rather than to make the local position information nonsingular. The general rank condition also covers geometries in which amplitude information alone is insufficient.

2.4 Choosing reference frequencies

We next examine which frequencies allow the reference to constrain phase at the sensing carrier. A single reference at a nonzero offset u_0 has $\mu = u_0$, $\nu = u_0^2$ and $\gamma = 0$. An unknown intercept and slope can compensate for each other at that frequency, so the reference supplies no carrier-phase information. The amplitude information $\mathbf{J}_A$ remains.

This compensation can be written explicitly. For a change from $\mathbf{x}$ to $\mathbf{x}'$, let $\Delta\boldsymbol{\delta} = \boldsymbol{\delta}(\mathbf{x}') - \boldsymbol{\delta}(\mathbf{x})$ and set $\boldsymbol{\psi}' = \boldsymbol{\psi} + k_0 \Delta\boldsymbol{\delta}$ and $\boldsymbol{\chi}' = \boldsymbol{\chi} - k_0 \Delta\boldsymbol{\delta}/u_0$. These changes preserve the sensing phases and the reference phases at u_0. The sensing magnitudes generally change, however. Preserving the full complex response would also require the vectors $[A_m(\mathbf{x})]$ and $[A_m(\mathbf{x}')]$ to coincide after adjusting the common gain. Preserving phases alone is therefore insufficient to show a position ambiguity in this model.



(a) **(b)**

Figure 1: Phase references improve accuracy even when amplitudes provide full local rank. a: A twelve-sensor line array with measured pairs $(1, 5)$ and $(8, 12)$. **b:** Local PEB along bearing 74° at fixed sensing SNR 10, without references, with one pair, and with both disconnected pairs. Each active pair receives reference SNR 5 at bracketing frequencies. Adding a pair increases the total budget, so these curves show the information added by calibration. Equal-budget designs are compared in Figure 3. Relative amplitudes make the local information nonsingular in all three cases.

A carrier-only reference has $\gamma = 1$, although it does not identify the delay slopes. References with weighted mean offset zero also have $\gamma = 1$. Both estimate the carrier phase without a local information penalty from the unknown slopes. The two-tone rule below concerns prescribed reference frequencies that may lie away from the sensing carrier.

With two fixed reference frequencies, their SNR weights determine how well the carrier phase is separated from the slope. Maximizing γ gives the classical two-point rule for estimating an intercept [18].

Proposition 3. *For distinct fixed normalized offsets $a < b$, the largest carrier-phase information fraction is*

$$\gamma_{\max} = \frac{(b-a)^2}{(|a|+|b|)^2}, \qquad w_a = \frac{|b|}{|a|+|b|}, \quad w_b = 1 - w_a. \tag{15}$$

A pair bracketing the carrier attains $\gamma_{\max} = 1$. If one offset is zero, the formula assigns all reference SNR to that carrier tone. The weight optimization is given in Section 4.1.4.

At fixed sensing and pair SNRs, increasing γ cannot decrease $\mathbf{W}$ in the positive semidefinite order. The calibrated phase contribution therefore cannot decrease, while the amplitude contribution remains unchanged. This frequency rule assumes phase varies affinely with frequency and every pair uses the same frequency weights. Nonlinear phase responses or frequency-dependent measurement costs would require a different design.

For a complete graph with equal pair weights, $\mathbf{L} = 2Q\mathbf{C}/(N-1)$. Even in this case, the best sensing/calibration split depends on the geometry through the unequal sensor powers and the amplitude term $\mathbf{J}_A$. We therefore optimize the split using the full position bound. If $\gamma = 0$ and the amplitude information is nonsingular, the best allocation puts all resources into sensing because the references add no position information. Figure 2 illustrates how frequency placement and the sensing/calibration split affect positioning. Panel a shows the maximum carrier-phase information fraction for two reference tones, including the interval where they bracket the sensing carrier. Panel b shows the resulting trade-off between sensing and calibration under a fixed total received-SNR budget, with calibration SNR divided equally among all sensor pairs.

2.5 Allocating SNR between sensing and calibration

Once the reference frequencies are fixed, we choose how much SNR to assign to sensing and to each sensor pair. A joint FIM makes this optimization easier because it depends linearly on these resources.

The zero-sum space $\mathbf{1}^\perp = \{\mathbf{z} : \mathbf{1}^T\mathbf{z} = 0\}$ describes relative phases after removing the common phase. Let $\mathbf{U} \in \mathbb{R}^{N\times(N-1)}$ have orthonormal columns spanning this space. Define $\mathbf{H} = \mathbf{U}^T\mathbf{G}$, $\mathbf{K}_b = \mathbf{U}^T\mathbf{K}\mathbf{U}$ and $\mathbf{L}_b = \mathbf{U}^T\mathbf{\Lambda}\mathbf{U}$. In these coordinates the joint position and hardware-phase FIM is

$$\mathcal{J} = \begin{bmatrix} \mathbf{J}_A + k_0^2\mathbf{H}^T\mathbf{K}_b\mathbf{H} & -k_0\mathbf{H}^T\mathbf{K}_b \\ -k_0\mathbf{K}_b\mathbf{H} & \mathbf{K}_b + \mathbf{L}_b \end{bmatrix}. \tag{16}$$

The matrix $\mathcal{J} \in \mathbb{R}^{(d+N-1)\times(d+N-1)}$ concerns position and the $N-1$ relative-phase coordinates $\mathbf{U}^T\boldsymbol{\psi}$. The common hardware phase has been absorbed by the unknown gain. The gain magnitude and the delay slopes have already been eliminated.

Choose a set of M anticipated source positions, $\Omega = \{\mathbf{x}_r\}_{r=1}^M$, before acquisition. This set represents where the source is expected to lie; its actual position remains unknown. The matrix $\mathbf{E} = [\mathbf{I}_d\ \mathbf{0}]^T \in \mathbb{R}^{(d+N-1)\times d}$ selects the position coordinates. Minimize

$$F(S, \mathbf{q}) = \frac{1}{M}\sum_{r=1}^{M} \mathrm{tr}[\mathbf{E}^T\mathcal{J}(\mathbf{x}_r; S, \mathbf{q})^{-1}\mathbf{E}], \tag{17}$$

$$S + \mathbf{1}^T\mathbf{q} = T, \qquad S \geq 0, \quad \mathbf{q} \geq 0. \tag{18}$$

At each design position, the selected inverse block is $\mathbf{J}_{\mathbf{x}}^{-1}$, so its trace equals $\mathrm{PEB}(\mathbf{x}_r)^2$. Thus F is the average squared PEB and $\sqrt{F}$ is the root-mean-square PEB over the design set. We report this RMS value, rather

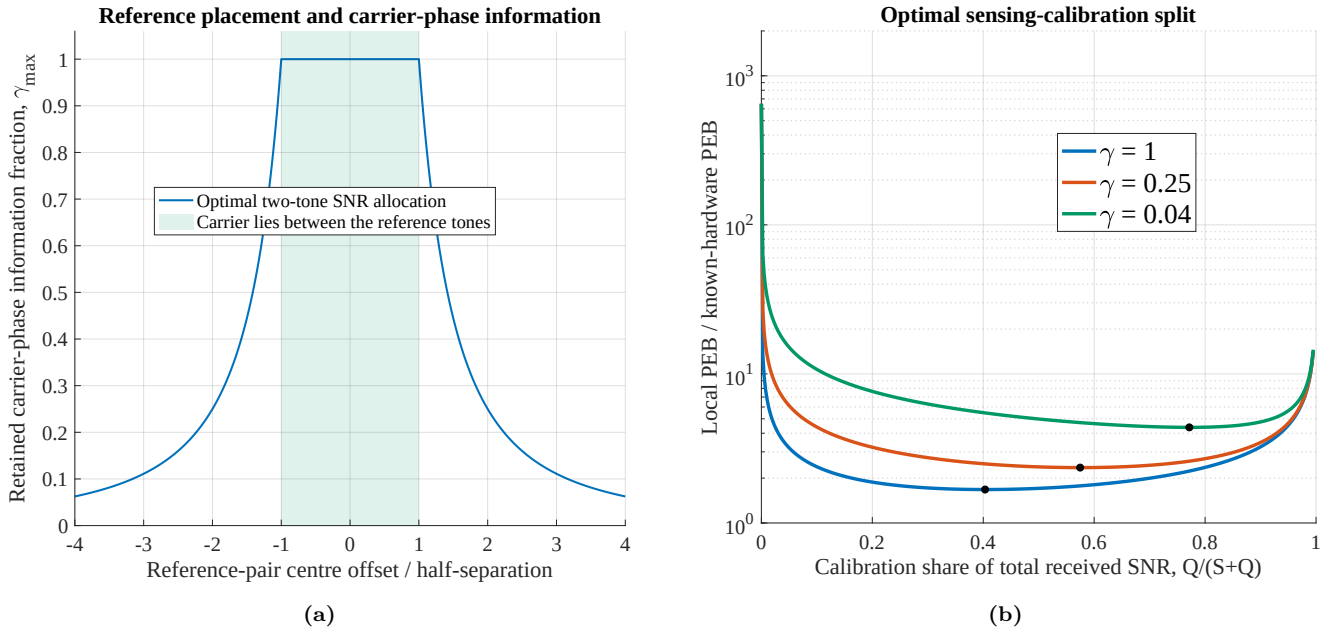


Figure 2: Reference frequencies and calibration share both affect accuracy. a: Maximum fraction of carrier-phase information retained with two reference tones of fixed separation. The horizontal coordinate is the pair's centre offset from the sensing carrier, divided by the tones' half-separation. The reference SNR is optimally divided between the tones at each centre position. Shading marks positions where the carrier lies between the tones; there, the fraction equals one. **b:** Local position-error bound at the held-out position $r = 6.4\,\mathrm{m}$, $\theta = 74^\circ$ as a function of the calibration share of a fixed total received SNR. Calibration SNR is divided equally among all sensor pairs. Each curve uses the indicated carrier-phase information fraction γ. The bound is divided by the bound for known hardware with the full budget assigned to sensing. Circular markers indicate the minimum of each curve.

than the arithmetic average of the PEBs. Singular position information is assigned infinite objective. The criterion averages local variance over the selected positions; accuracy elsewhere in the region must be checked separately.

Convexity allows us to compare a computed allocation with the best one in this design family. Write the resource fractions as $\mathbf{w} = (S, \mathbf{q}^T)^T/T$, and let $\mathbf{g} = \nabla_{\mathbf{w}} F(T\mathbf{w})$ be the objective gradient with respect to these fractions. The frequency weights w_ℓ remain fixed. Let F^* denote the optimal objective value.

Proposition 4. *For fixed design positions, reference frequencies and $T > 0$, (17)-(18) is convex wherever the objective is finite. At a finite design, the Frank-Wolfe gap*

$$g_{\mathrm{FW}} = \mathbf{g}^T\mathbf{w} - \min_i g_i \tag{19}$$

satisfies $F - g_{\mathrm{FW}} \le F^* \le F$, where g_i is component i of $\mathbf{g}$.

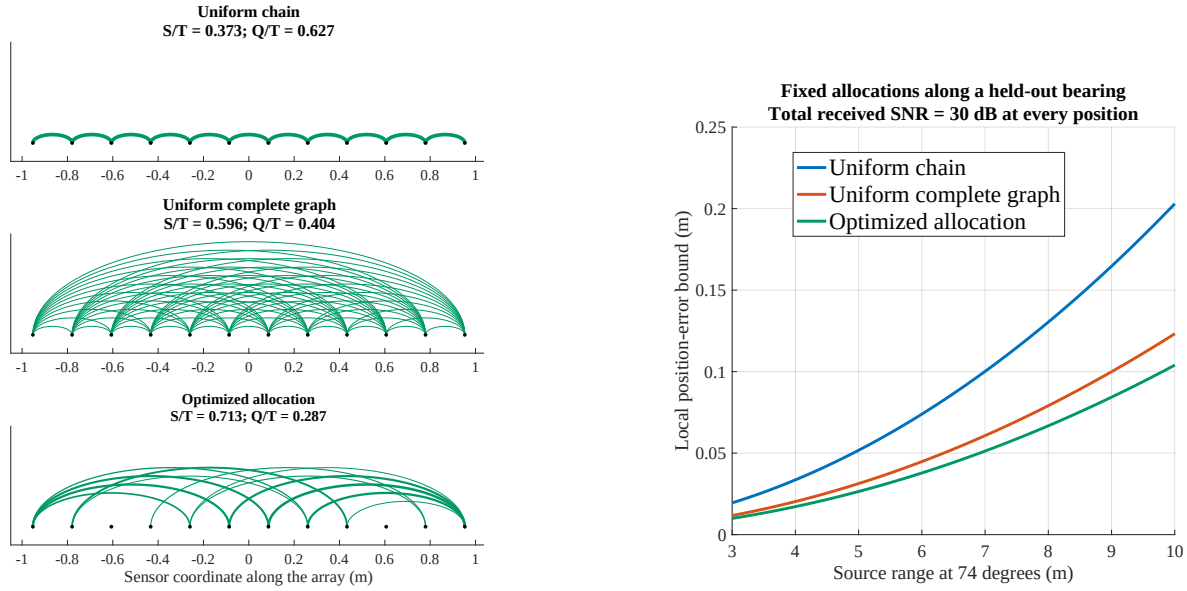
Convexity follows from the affine dependence of the joint FIM on the allocated SNRs. The proof and the derivation of the gap bound are given in Section 4.1.5.

The fractions are nonnegative and sum to one, so they form a simplex. At each Frank-Wolfe step, the smallest gradient component selects sensing or one reference pair. The algorithm moves partway towards putting all the budget into that component. The gap bounds the possible improvement in the design objective. Scaling all resources by T scales the information by T and the variance objective by $1/T$, so the optimal fractions stay the same under this received-SNR convention. Figure 3 compares the uniform chain, uniform complete graph and optimized allocation. Panel a shows how each design distributes calibration SNR among sensor pairs, with its sensing share optimized separately. Panel b compares their position-error bounds along a held-out bearing, using the same total received SNR and keeping each allocation fixed as the source range varies.

2.6 Numerical bounds and position estimates

We now compare the allocation with uniform calibration graphs and test the resulting designs using complex observations. We use $N = 12$ sensors equally spaced over a 1.905 m line aperture, carrier 10 GHz and propagation speed 3×10^8 m/s. The design set combines ranges $4, 6, 8$ m with bearings $50^\circ, 70^\circ, 90^\circ, 110^\circ$, measured from the positive array axis. All 66 sensor pairs are candidates. We set $B_r = 100$ MHz. The reference frequencies 9.9 and 10.1 GHz therefore have normalized offsets -1 and 1. Equal SNR weights on these tones give $\gamma = 1$. The complete-graph baseline uses every pair; the chain baseline uses only adjacent sensor indices $(m, m+1)$. Each uniform baseline divides reference SNR equally over its active edges and optimizes its sensing share. The designed allocation also optimizes individual edge weights.

At unit total received SNR, the region-average squared PEB is 10.6654, 3.9301 and 2.8151 m^2 for the chain, complete graph and designed allocation. Their sensing shares are 0.3725, 0.5964 and 0.7133. The resulting root-mean-square bound reductions are 15.37% and 48.62% relative to the complete graph and chain. All



(a) **(b)**

Figure 3: Allocation uses the full amplitude and phase model. a: Pairwise calibration allocations for a uniform chain, a uniform complete graph and an optimized allocation over twelve design positions. Black dots denote receive sensors; green arcs denote calibrated pairs. Each design has its own optimized sensing share. Arc width indicates pair SNR relative to the largest pair SNR within that panel. For legibility, arcs with less than 2% of the largest pair weight are omitted from the drawing. **b:** Local position-error bound along the held-out bearing 74°, using the fixed allocations in panel a. The source range varies from 3 to 10 m; the total received SNR is held at 30 dB at each position. The allocations are not reoptimized along this path.

reported values use inverse-distance amplitudes. After 1800 Frank-Wolfe steps, the relative gap is 0.00225. Its certificate places the objective within 0.226% of the optimum in the stated finite design family.

Amplitude-only information is positive definite at every design point, but is weak: assigning the full unit received-SNR budget to sensing without references gives a region-average squared PEB of 659980 m^2. Thus full local rank alone does not imply useful accuracy. This comparison assumes known relative receiver magnitude gains.

We simulate independent complex observations at the held-out position $r = 6.4$ m, bearing 74°. A common coarse search box $[1.5, 2.5] \times [5.5, 6.5]$ m is given to every receiver. The coarse search region is assumed to be available before fine positioning. Obtaining this region from acquisition measurements is outside the present study. A standard joint likelihood fit estimates position, hardware phase and slope, and complex gain. A sequential comparator first fits reference phases and then position. Every trial is retained.

Figure 4 compares position root-mean-square error (RMSE) across 120 paired trials per condition at total received SNRs from 20 to 40 dB. Over this interval, the joint-fit RMSE decreases from 0.2652 to 0.02622 m for the uniform chain, from 0.1885 to 0.01707 m for the uniform complete graph, and from 0.1452 to 0.01389 m for the optimized allocation. The optimized allocation has the lowest empirical RMSE at each tested SNR. Both the simulated observations and the receiver use the same spherical-spreading model. Performance under propagation or hardware-model mismatch requires separate evaluation.

The local PEB applies to locally unbiased estimation. The receiver uses a bounded search region and may be biased, so its RMSE is not required to exceed this bound. Finite-trial variation also affects the comparison. The simulations assess performance within the stated coarse region.

3 Discussion

The results demonstrate that calibration requirements for near-field positioning should be evaluated in terms of their contribution to positioning accuracy, rather than solely through the accuracy of recovered hardware parameters. Specifically, the amplitude and phase terms answer two different questions about calibration. Known relative receiver gains allow amplitude ratios to constrain position even when phase references are uninformative. This can give full local rank, as the line-array result shows. Useful accuracy is a separate matter: in the numerical example, the amplitude-only bound is large, and the phase references substantially improve it. Consequently, local identifiability does not necessarily imply that the available calibration is sufficient to achieve a desired positioning accuracy. A calibration requirement should therefore specify both the hardware assumptions and the desired accuracy.

The magnitude assumption is essential. Suppose each channel has an arbitrary unknown positive magnitude gain h_m, and the reference measurements provide no information about these gains. The received sensing-

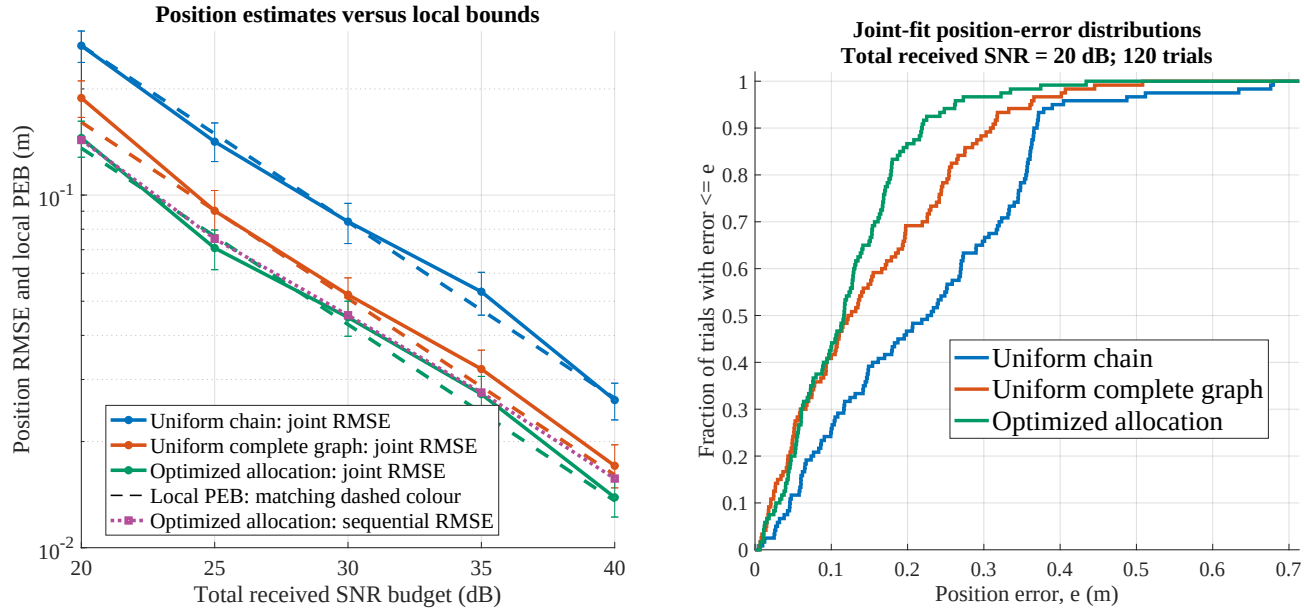


Figure 4: Receiver errors under the spherical-spreading model. a: Position RMSE from 120 synthetic complex-data trials per SNR at the held-out source position $r = 6.4\,\mathrm{m},\ \theta = 74^\circ$. Solid curves show a joint fit of position and hardware parameters for the three fixed allocations in Fig. 3a; matching dashed curves show their local position-error bounds. The dotted curve shows a sequential calibration-then-position fit with the optimized allocation. The horizontal axis is the sum of received sensing and calibration SNRs. **b:** Empirical cumulative distributions of joint-fit position error from all 120 trials at total received SNR 20 dB, using the fixed allocations in Fig. 3a. At each error threshold, the curve gives the fraction of trials with error at or below that threshold. The source is at $r = 6.4\,\mathrm{m},\ \theta = 74^\circ$.

power fractions are then

$$\widetilde{\omega}_m = \frac{h_m^2 r_m^{-2}}{\sum_n h_n^2 r_n^{-2}}, \qquad \widetilde{\boldsymbol{\omega}} = [\widetilde{\omega}_1, \ldots, \widetilde{\omega}_N]^T.$$

Let $\mathbf{v} = \Delta\mathbf{x}$ be a small source displacement and $\zeta_m = \Delta \log h_m$ a logarithmic gain perturbation. Since the unnormalized amplitude is proportional to h_m/r_m,

$$\Delta \log(h_m/r_m) = \zeta_m + \mathbf{R}_{m,:}\mathbf{v}.$$

Choosing $\zeta_m = -\mathbf{R}_{m,:}\mathbf{v}$ cancels the amplitude change at every sensor. The unknown common gain also absorbs any change arising from amplitude normalization. Eliminating the sensor gains therefore removes the amplitude contribution to position information.

The remaining phase information retains the form $k_0^2\mathbf{G}^T\mathbf{W}\mathbf{G}$, evaluated using

$$\mathbf{K} = 2S\left[\mathrm{diag}(\widetilde{\boldsymbol{\omega}}) - \widetilde{\boldsymbol{\omega}}\widetilde{\boldsymbol{\omega}}^T\right],$$

where S is the actual total received sensing SNR in this extended model. For $\gamma > 0$, the position-rank condition reduces to $\mathrm{rank}(\mathbf{B}_{\mathcal{A}}\mathbf{G}) = d$. A single off-carrier reference gives $\gamma = 0$ and therefore leaves no local position information in this single-source, single-carrier model. Retaining amplitude information thus requires constraints on the relative receiver magnitude gains. Unknown gains and phases have been studied previously [12, 27].

For measurement design, we first choose reference frequencies that retain information about phase at the sensing carrier. We then check whether the amplitude and calibrated phase changes constrain all position coordinates, and allocate SNR to minimize the position bound. The value of a reference pair depends on both the array geometry and the source region. This geometry dependence explains why calibration measurements that are effective for estimating receiver phase differences are not necessarily the most valuable for positioning. The relevant design criterion is how much each measurement improves the position information after accounting for the remaining hardware uncertainties. This links calibration-graph analysis [15] with spherical-wave position bounds [8, 9] under an explicit reference model and budget. Compared with wideband calibration and experimental CSI correction [16, 17], the present results concern controlled reference paths and synthetic observations.

Applying the design to a physical array requires a suitable model of both sensing and calibration. Uncertain element patterns, polarization, mutual coupling, unequal noise and sensor-coordinate errors can change the information. The radiating point-source approximation also excludes reactive coupling close to an antenna. Multipath, extended or multiple sources, and time variation require additional parameters. Cables, couplers or a controlled radiator may provide the reference, but its path phase must be known to use (6). Unknown over-the-air paths, frequency-dependent reference amplitudes and nonlinear hardware phase responses require changes to the reference model and its frequency design.

The bounds describe local accuracy under the stated gain, propagation and reference assumptions. A line array has a reflection ambiguity unless the source half-plane is known. With at least three distinct sensor positions, exact amplitude ratios distinguish source positions within that half-plane. However, amplitude informa-

tion can be weak at finite SNR, and phase periodicity can create competing likelihood peaks. The simulations use a coarse search box and local optimization. Overall, the results illustrate how array calibration can evolve to support positioning as an emerging wireless service. Rather than treating calibration as an independent hardware characterization task, the proposed framework incorporates positioning accuracy directly into the selection and allocation of calibration measurements. Under the stated propagation and hardware assumptions, this positioning-oriented approach improves accuracy compared with uniform calibration strategies at the same received-SNR budget. It therefore provides a basis for extending established calibration practices towards the requirements of spatially aware wireless systems.

4 Methods

4.1 Analytical derivations

This section gives the proofs of the information formula, the geometry conditions, the reference-frequency rule and the convex allocation result.

4.1.1 Position information

We first prove Theorem 1 by eliminating the reference slopes, the common gain and the receiver phases.

Proof. For independent proper complex Gaussian samples of unit variance, the real-parameter FIM is twice the real part of the complex derivative Gram matrix [28]. For the references, the phase-phase, phase-slope and slope-slope blocks are $2\mathbf{L}$, $2\mu\mathbf{L}$ and $2\nu\mathbf{L}$, respectively. If $\nu > 0$, removing the slopes gives

$$2\mathbf{L} - (2\mu\mathbf{L})(2\nu\mathbf{L})^{\dagger}(2\mu\mathbf{L}) = 2(1-\mu^2/\nu)\mathbf{L}.$$

The pseudoinverse also covers disconnected graphs: $\mathbf{L}\mathbf{L}^{\dagger}\mathbf{L} = \mathbf{L}$, and the columns of the phase-slope block lie in the column space of $\nu\mathbf{L}$. If $\nu = 0$, all active offsets vanish, so the slope and cross blocks are zero and the remaining block is $2\mathbf{L}$.

Write $\alpha = \rho e^{j\vartheta}$ with $\rho > 0$. Let $\mathbf{v} = \Delta\mathbf{x}$, $\boldsymbol{\eta} = \Delta\boldsymbol{\psi}$ and $\tau = \Delta\vartheta$. At sensor m, the relative amplitude change is $\Delta\rho/\rho + (\mathbf{R}_{m,:} - \boldsymbol{\omega}^T\mathbf{R})\mathbf{v}$, and the phase change is $\tau + \eta_m - k_0\mathbf{G}_{m,:}\mathbf{v}$. These contribute separately to the Fisher quadratic form:

$$2S\sum_m \omega_m\Big[\big(\Delta\rho/\rho + (\mathbf{R}_{m,:} - \boldsymbol{\omega}^T\mathbf{R})\mathbf{v}\big)^2 + (\tau + \eta_m - k_0\mathbf{G}_{m,:}\mathbf{v})^2\Big].$$

The amplitude and phase terms have no cross term. The weighted mean of the normalized amplitude derivatives is zero, so minimizing over $\Delta\rho$ leaves $\mathbf{v}^T\mathbf{J}_A\mathbf{v}$. Minimizing over τ removes the weighted common phase and leaves

$$(\boldsymbol{\eta} - k_0\mathbf{G}\mathbf{v})^T\mathbf{K}(\boldsymbol{\eta} - k_0\mathbf{G}\mathbf{v}).$$

Adding the reference term gives the equivalent position quadratic form

$$\mathbf{v}^T\mathbf{J}_A\mathbf{v} + \min_{\boldsymbol{\eta}}\left\{\left\|\mathbf{K}^{1/2}(\boldsymbol{\eta} - k_0\mathbf{G}\mathbf{v})\right\|^2 + \left\|\boldsymbol{\Lambda}^{1/2}\boldsymbol{\eta}\right\|^2\right\}. \tag{20}$$

Both $\mathbf{K}$ and $\boldsymbol{\Lambda}$ map $\mathbf{1}$ to zero, reflecting the unobservable common phase. Since all sensor-power weights are positive, $\mathbf{K}$ is positive definite on $\mathbf{1}^{\perp}$. Thus $\ker(\mathbf{K}+\boldsymbol{\Lambda}) = \operatorname{span}\{\mathbf{1}\}$. Minimizing the quadratic form over $\boldsymbol{\eta}$ gives the generalized Schur complement in (13). □

4.1.2 Local rank condition

We use the variational expression above to prove Proposition 1.

Proof. The amplitude term in (20) vanishes precisely when $\mathbf{R}\mathbf{v}$ is constant across sensors, or $\mathbf{C}\mathbf{R}\mathbf{v} = 0$. The minimized phase term vanishes precisely when there is an $\boldsymbol{\eta}$ with $\boldsymbol{\eta} - k_0\mathbf{G}\mathbf{v} \in \operatorname{span}\{\mathbf{1}\}$ and $\boldsymbol{\Lambda}\boldsymbol{\eta} = 0$. For $\gamma > 0$, this is equivalent to $\mathbf{B}_{\mathcal{A}}\mathbf{G}\mathbf{v} = 0$. The total FIM is positive definite exactly when these two null conditions share no nonzero displacement. With $\boldsymbol{\Lambda} = 0$, every phase perturbation is absorbed and only the amplitude condition remains. □

4.1.3 Amplitude information for a line array

For the line-array geometry in Proposition 2, three distinct sensor positions suffice to establish the amplitude rank.

Proof. Suppose $\mathbf{C}\mathbf{R}\mathbf{v} = 0$, so $\mathbf{R}_{m,:}\mathbf{v} = \kappa$ for a common scalar $\kappa \in \mathbb{R}$. Write $\mathbf{v} = (v_x, v_y)^T$. With $t_m = x - s_m$, this gives

$$-v_x t_m - v_y y = \kappa(t_m^2 + y^2).$$

The polynomial $\kappa t^2 + v_x t + \kappa y^2 + v_y y$ has at least three distinct roots. It is therefore identically zero: $\kappa = v_x = 0$ and $v_y y = 0$. Since $y \neq 0$, $\mathbf{v} = 0$. The amplitude rank condition follows. □

4.1.4 Reference-frequency weights

For Proposition 3, the reference frequencies are fixed and only their SNR weights are varied.

Proof. For weight $p \in [0,1]$ on a, $\nu - \mu^2 = p(1-p)(b-a)^2$. Maximizing $p(1-p)(b-a)^2/[pa^2 + (1-p)b^2]$ gives the stated weight when $ab \neq 0$. For bracketing offsets, it also makes $\mu = 0$. A zero offset gives the endpoint solution directly under the $\nu = 0$ convention. □

4.1.5 Convex allocation and the optimality gap

To establish Proposition 4, we use the joint FIM and the supporting-hyperplane inequality for a convex objective.

Proof. At each fixed position, $\boldsymbol{\omega}$ and $\mathbf{R}$ are fixed and $\mathbf{K} = 2S\mathbf{P}_{\omega}$ is linear in S. The reference matrix is linear in $\mathbf{q}$, so (16) is affine in all resources. For design position $\mathbf{x}_r$, write $\mathcal{J}_r = \mathcal{J}(\mathbf{x}_r; S, \mathbf{q})$ and introduce an auxiliary symmetric matrix $\mathbf{Y}_r \in \mathbb{R}^{d\times d}$. An upper bound on the selected inverse block is expressed by

$$\begin{bmatrix} \mathcal{J}_r & \mathbf{E} \\ \mathbf{E}^T & \mathbf{Y}_r \end{bmatrix} \succeq 0.$$

Minimizing average $\operatorname{tr}\mathbf{Y}_r$ gives the usual convex matrix-fractional formulation [19, Example 3.4]. For $S > 0$, the

lower hardware block is positive definite, so invertibility is equivalent to positive-definite position information. Designs with $S = 0$ have no position information and infinite objective.

Convexity gives $F(T\mathbf{w}') \geq F(T\mathbf{w}) + \mathbf{g}^T(\mathbf{w}' - \mathbf{w})$ for any other feasible allocation $\mathbf{w}'$. Its linear minimum occurs at a vertex with smallest gradient component. Minimizing this lower bound proves (19) and the certificate [20]. □

4.2 Stable evaluation of the information

The sensors lie at $(s_m, 0)$ with s_m equally spaced on $[-0.9525, 0.9525]$ m. We evaluate the analytic derivatives in (1) and (8) without a Fresnel expansion. For brevity, let $a_m = [\mathbf{a}_{\mathrm{NF}}(\mathbf{x})]_m$. The normalized steering derivative used in the receiver is

$$\nabla_{\mathbf{x}}^T a_m = a_m[\mathbf{R}_{m,:} - \boldsymbol{\omega}^T\mathbf{R} - jk_0\mathbf{G}_{m,:}]. \tag{21}$$

The term $-\boldsymbol{\omega}^T\mathbf{R}$ accounts for the position dependence of the amplitude normalization. It must be retained when differentiating the steering vector.

When reference information is weak, the two terms defining $\mathbf{W}$ can nearly cancel numerically. We avoid this subtraction by working in zero-sum coordinates. Define

$$\mathbf{Z} = (\mathbf{K}_b + \mathbf{L}_b)^{-1}\mathbf{K}_b\mathbf{H}, \quad \mathbf{V} = (\mathbf{K}_b + \mathbf{L}_b)^{-1}\mathbf{L}_b\mathbf{H}. \tag{22}$$

Here $\mathbf{Z} + \mathbf{V} = \mathbf{H}$. We evaluate the information as a sum of positive semidefinite terms:

$$\mathbf{J}_{\mathbf{x}} = \mathbf{J}_A + k_0^2(\mathbf{V}^T\mathbf{K}_b\mathbf{V} + \mathbf{Z}^T\mathbf{L}_b\mathbf{Z}). \tag{23}$$

It follows by substituting the minimizing hardware perturbation into (20). We report an infinite PEB if the smallest eigenvalue is at most 10^{-11} times the largest. This numerical threshold is separate from the exact rank condition.

4.3 Optimization and derivatives

We optimize normalized resources at $T = 1$. Each uniform baseline uses a bounded scalar search over its sensing share and also checks the all-sensing endpoint. Frank-Wolfe starts from the optimized complete-graph design, chooses the smallest gradient component, and performs a bounded line search. The stopping conditions are relative gap 5×10^{-4} or 1800 iterations. The run reaches the iteration limit, so the reported certificate uses its achieved gap.

Let ξ_i denote one scalar resource, either S or one pair budget q_e. With $\mathcal{J}_r = \mathcal{J}(\mathbf{x}_r)$, the analytic gradient is

$$\frac{\partial F}{\partial \xi_i} = -\frac{1}{M}\sum_r \mathrm{tr}\left[\mathbf{X}_r^T\frac{\partial \mathcal{J}_r}{\partial \xi_i}\mathbf{X}_r\right], \quad \mathbf{X}_r = \mathcal{J}_r^{-1}\mathbf{E}. \tag{24}$$

The normalized gradient is $g_i = T\,\partial F/\partial \xi_i$. The code evaluates an equivalent residual expression with separate amplitude and phase contributions. All pair weights enter the objective, including the small weights hidden in the graph drawing. The optimization allows any number of active pairs and has no sparsity penalty.

4.4 Synthetic data and receiver

Hardware phases are generated in zero-sum coordinates: entries of $\mathbf{U}^T\boldsymbol{\psi}$ and $\mathbf{U}^T\boldsymbol{\chi}$ are independent Gaussian variables with standard deviations 0.3 and 0.12 radians. The common gain magnitude is $\sqrt{S/N}$ with independent phase uniform on $[-\pi, \pi]$. These distributions are used only to generate the synthetic hardware. The estimator and FIM treat the hardware parameters as unknown deterministic quantities. Each complex noise has independent real and imaginary parts of variance 1/2. We use MATLAB's Mersenne Twister generator with seed $426000 + 1000i + j$, where i and j are the zero-based SNR and trial indices. The same seed is used across allocations to pair the hardware and noise realizations.

For the allocated reference SNRs, the joint fit minimizes the negative log-likelihood up to an additive constant:

$$\mathcal{L} = \|\mathbf{y} - \alpha\mathbf{D}(\boldsymbol{\psi})\mathbf{a}_{\mathrm{NF}}(\mathbf{x})\|^2 + \sum_{e,\ell}\left|z_{e\ell} - \sqrt{q_e w_\ell}e^{j\mathbf{b}_e^T(\boldsymbol{\psi} + u_\ell\boldsymbol{\chi})}\right|^2. \tag{25}$$

We constrain position to the stated coarse box and impose $\mathbf{1}^T\boldsymbol{\psi} = \mathbf{1}^T\boldsymbol{\chi} = 0$. The latter conditions choose coordinates for the unobservable common phase and common slope; they add no calibration information. The common gain α is still estimated. For fixed position and hardware phase, its least-squares value is

$$\widehat{\alpha} = \frac{\mathbf{a}_{\mathrm{NF}}(\mathbf{x})^H\mathbf{D}(\boldsymbol{\psi})^H\mathbf{y}}{N}. \tag{26}$$

When evaluating the coarse position grid and refining the sequential position estimate, we compute the gain from (26) at each candidate position. The resulting gain estimate also initializes the joint fit. The joint fit then estimates the real and imaginary parts of α together with position and hardware parameters.

We initialize the hardware phases and slopes by amplitude-weighted linear least squares on the wrapped reference angles. This works for the small hardware errors used here. Larger errors may require phase unwrapping before initialization. A 13×13 grid over the common coarse box selects three positions using the likelihood score after profiling the common gain. The sequential receiver refines position with fixed estimated hardware. The joint receiver then fits the real and imaginary sensing and reference residuals, including the normalized amplitude derivative. Of the three fits, we retain the one with the lowest final negative log-likelihood. The true position is used only to compute errors afterwards.

For each of the three selected starting positions, the MATLAB implementation refines position with the hardware parameters fixed. The refined position, reference-based hardware estimates and gain from (26) initialize a joint fit using damped Gauss-Newton iterations with an analytic residual Jacobian. The joint iterations constrain position to the same box and update position, hardware phases, delay slopes and complex gain. The optimization is local and may miss the global likelihood

optimum. Reported RMSE is the square root of the mean squared Euclidean position error, using every trial.

4.5 Independent checks and reproducibility

The MATLAB validation routine checks (13) against an independent construction of the full complex observation Jacobian. It stacks the real and imaginary parts and multiplies them by $\sqrt{2}$ to account for the unit complex noise variance. Projecting out the gain, phase and slope columns gives a second calculation of the position FIM.

The routine includes 32 cases covering random arrays, disconnected or empty calibration graphs, carrier-only, bracketing, same-side and single off-carrier references, and on-axis line-array geometries. It compares the information matrices, checks the amplitude-only limit and tests the combined rank condition. A separate nuisance projection checks the loss of amplitude information when every sensor magnitude is unknown.

Central differences check the normalized steering derivative, the resource gradient and the receiver residual Jacobian. A dense weight search checks the two-frequency rule. Additional checks test steering-vector normalization, budget scaling and the uniform chain and complete-graph design benchmarks. These checks test agreement between the implementation, analytical expressions and limiting cases. The proofs in Section 4.1 establish the analytical results.

All reported figures and numerical results were generated using MATLAB 2022b. The implementation requires MATLAB R2019a or later and no specialist toolboxes. The supplied function returns figure handles and numerical results, including simulated observations, position estimates, trial errors, seeds and optimization history.

Data availability

Supplementary Data 1 contains the synthetic sensing and reference observations, position estimates, trial errors, figure source data, optimization history and MATLAB results supporting the reported numerical experiments.

Code availability

The MATLAB code used to generate the reported figures and numerical results is provided in Supplementary Software 1 under the MIT license. The package includes execution instructions, model parameters and numerical validation checks.

Acknowledgments

This work is supported in part by Digital Futures and the EU Horizon projects MULTIPLY-6G and QUEST-6G under Project IDs 101293106 and 101292676, respectively. G. Fodor was also supported by SSF grant FUS21-0004 SAICOM.

Author contributions

S.D. initiated the study and prepared the original manuscript. G.F. contributed to the conceptual development, interpretation of the results and manuscript revision. M.S. edited the manuscript. All authors reviewed and approved the final manuscript.

Competing interests

The authors declare no financial or non-financial competing interests.

References

[1] Ayman Elnashar, Marwan Bin Shakar, Hadi Otrok, Azzam Mourad, Shimaa Naser, and Sami Muhaidat. AI-native 6G networks: A comprehensive survey on architecture, enabling technologies, functional capabilities, and the path to autonomous connectivity. *IEEE Open Journal of the Communications Society*, pages 1–1, 2026. doi: 10.1109/OJCOMS.2026.3742848.

[2] Ruiqi Liu, Leyi Zhang, Minqiang Zou, Sergio Parolari, and Li Tian. Evaluating radio interfaces toward 6G: What's new and what's different. *IEEE Network*, 39(6): 148–154, 2025. doi: 10.1109/MNET.2025.3557403.

[3] Liang Ma, Marc Grant, Hui Lin, Johan Sköld, Ruiqi Liu, and Jiafeng Shao. From vision to design targets: Technical performance requirements for IMT-2030. *IEEE Communications Magazine*, 64(6):6–9, 2026. doi: 10.1109/MCOM.2026.11550739.

[4] Qingji Jiang, Jing Jin, Qixing Wang, Yuanyuan Tang, Yang Cao, Bin Kuang, Jing Dong, Siying Lv, Dongming Wang, Yongming Huang, Jiangzhou Wang, and Xiaohu You. Experimental performance of bidirectional phase coherent transmission and sensing for mmwave cell-free massive MIMO systems with reciprocity calibration. *IEEE Journal on Selected Areas in Communications*, 44:3591–3607, 2026. doi: 10.1109/JSAC.2026.3664828.

[5] Qingqing Tang, Xiangyue Wei, Dong Tang, and Yue Li. Near-field communications for 6G: Applications, characteristics, and deployment strategies. *IEEE Network*, 39(6):14–20, 2025. doi: 10.1109/MNET.2025.3599375.

[6] Jiayi Cong, Changsheng You, Jiapeng Li, Li Chen, Beixiong Zheng, Yuanwei Liu, Wen Wu, Yi Gong, Shi Jin, and Rui Zhang. Near-field integrated sensing and communication: Opportunities and challenges. *IEEE Wireless Communications*, 31(6):162–169, 2024. doi: 10.1109/MWC.002.2400033.

[7] Siwei Zhang, Thomas Jost, Robert Pöhlmann, Armin Dammann, Dmitriy Shutin, and Peter A. Hoeher. Spherical wave positioning based on curvature of arrival by an antenna array. *IEEE Wireless Communications Letters*, 8(2):504–507, 2019. doi: 10.1109/LWC.2018.2877971.

[8] Youcef Begriche, Messaoud Thameri, and Karim Abed-Meraim. Exact conditional and unconditional Cramér–Rao bounds for near field localization. *Digital Signal Processing*, 31:45–58, 2014.

[9] Jin He, Linna Li, and Ting Shu. Bearing and range estimation with an exact source-sensor spatial model. *IET Signal Processing*, 14(9):614–623, 2020. doi: 10.1049/iet-spr.2020.0229.

[10] Houcem Gazzah and Jean Pierre Delmas. CRB-based design of linear antenna arrays for near-field source localization. *IEEE Transactions on Antennas and Propagation*, 62(4):1965–1974, 2014. doi: 10.1109/TAP.2014.2298882.

[11] Henk Wymeersch. A Fisher information analysis of joint localization and synchronization in near field. In *Proceedings of the IEEE International Conference on Communications Workshops (ICC Workshops)*, pages 1–6, 2020. doi: 10.1109/ICCWorkshops49005.2020.9145059.

[12] Jin He, Ting Shu, Linna Li, and Trieu-Kien Truong. Mixed near-field and far-field localization and array calibration with partly calibrated arrays. *IEEE Transactions on Signal Processing*, 70:2105–2118, 2022. doi: 10.1109/TSP.2022.3168975.

[13] Krishnaprasad Nambur Ramamohan, Sundeep Prabhakar Chepuri, Daniel Fernandez Comesana, and Geert Leus. Self-calibration of acoustic scalar and vector sensor arrays. *IEEE Transactions on Signal Processing*, 71:61–75, 2023. doi: 10.1109/TSP.2022.3214383.

[14] Long Yang, Xianghao Hou, and Yixin Yang. Self-calibration for sparse uniform linear arrays with unknown direction-dependent sensor phase by deploying an individual standard sensor. *Electronics*, 12(1):60, 2023. doi: 10.3390/electronics12010060.

[15] Erik G. Larsson. Massive synchrony in distributed antenna systems. *IEEE Transactions on Signal Processing*, 72:855–866, 2024. doi: 10.1109/TSP.2024.3358618.

[16] Yibo Wu, Musa Furkan Keskin, Ulf Gustavsson, Gonzalo Seco-Granados, Erik G. Larsson, and Henk Wymeersch. Location and map-assisted wideband phase and time calibration between distributed antennas. In *2024 IEEE Globecom Workshops (GC Wkshps)*, 2024. doi: 10.1109/GCWkshp64532.2024.11100563. Updated author version: arXiv:2410.23120v3, 2025.

[17] Qing Zhang, Adham Sakhnini, Robbert Beerten, Haoqiu Xiong, Zhuangzhuang Cui, Yang Miao, and Sofie Pollin. Robust localization in OFDM-based massive MIMO through phase offset calibration. In *2026 IEEE 6th International Symposium on Joint Communications and Sensing (JC&S)*, 2026. doi: 10.1109/JCS69321.2026.11366003.

[18] Gustav Elfving. Optimum allocation in linear regression theory. *The Annals of Mathematical Statistics*, 23(2):255–262, 1952. doi: 10.1214/aoms/1177729442.

[19] Stephen Boyd and Lieven Vandenberghe. *Convex Optimization*. Cambridge University Press, 2004.

[20] Martin Jaggi. Revisiting Frank–Wolfe: Projection-free sparse convex optimization. In *Proceedings of the 30th International Conference on Machine Learning*, volume 28 of *Proceedings of Machine Learning Research*, pages 427–435, 2013. URL https://proceedings.mlr.press/v28/jaggi13.html.

[21] Sajad Daei, Gábor Fodor, and Mikael Skoglund. When near becomes far: From Rayleigh to optimal near-field and far-field boundaries. In *GLOBECOM 2025 – IEEE Global Communications Conference*, pages 3586–3592, 2025.

[22] Sajad Daei, Gabor Fodor, and Mikael Skoglund. Living off the grid: Continuous range-angle super-resolution for near-field XL-MIMO. arXiv:2604.10234, 2026.

[23] Sajad Daei, Gábor Fodor, and Mikael Skoglund. Convexity meets curvature: Lifted near-field super-resolution. arXiv:2602.14063, 2026.

[24] Sajad Daei, Amirreza Zamani, Saikat Chatterjee, Mikael Skoglund, and Gábor Fodor. Near-field ISAC in 6G: Addressing phase nonlinearity via lifted super-resolution. In *2025 IEEE International Conference on Acoustics, Speech and Signal Processing (ICASSP)*, 2025. Author version: arXiv:2410.04930.

[25] Sajad Daei, Gábor Fodor, and Mikael Skoglund. A mathematical theory of near-field super-resolution. arXiv:2609.31299, 2026.

[26] Gilles Monnoyer, Jerome Louveaux, Laurence Defraigne, Baptiste Sambon, and Luc Vandendorpe. Aliasing in near-field array ambiguity functions: A spatial frequency-domain framework. *npj Wireless Technology*, 2:21, 2026. doi: 10.1038/s44459-026-00043-0.

[27] Han Cui, Wenjuan Peng, Tong Liu, and Xiaohui Wei. Cramér–Rao bounds for multiple near field sources location under unknown gain/phase response. In *2017 29th Chinese Control And Decision Conference (CCDC)*, 2017. doi: 10.1109/CCDC.2017.7979413.

[28] Olivier Besson and Yuri I. Abramovich. On the Fisher information matrix for multivariate elliptically contoured distributions. *IEEE Signal Processing Letters*, 20(11):1130–1133, 2013. doi: 10.1109/LSP.2013.2281914.

Supplementary Files

This is a list of supplementary files associated with this preprint. Click to download.

- supplemanterymaterial1npj.zip